Implementing an empirical scalar tertiary anisotropic rheology (ESTAR) into large-scale ice sheet models

Felicity S. Graham[1], Mathieu Morlighem[2], Roland C. Warner[3], and Adam Treverrow[3]

[1]Institute for Marine and Antarctic Studies, University of Tasmania, Private Bag 129, Hobart, Tasmania 7001, Australia
[2]Department of Earth System Science, University of California, Irvine, California, USA
[3]Antarctic Climate and Ecosystems Cooperative Research Centre, Private Bag 80, Hobart, Tasmania 7001, Australia

Correspondence to: Felicity S. Graham (felicity.graham@utas.edu.au)

Abstract. The microstructural evolution that occurs in polycrystalline ice during deformation leads to the development of anisotropic rheological properties that are not adequately described by the most common, isotropic, ice flow relation used in large-scale ice sheet models – the Glen flow relation. We present a preliminary assessment of the implementation in the Ice Sheet System Model (ISSM) of a computationally-efficient, empirical, scalar, tertiary, anisotropic rheology (ESTAR). The

5 effect of this anisotropic rheology on ice flow dynamics is investigated by comparing idealised simulations using ESTAR with those using the isotropic Glen flow relation, where the latter includes a flow enhancement factor. For an idealised embayed ice shelf, the Glen flow relation overestimates velocities by up to 17% when using an enhancement factor equivalent to the maximum value prescribed by ESTAR. Importantly, no single Glen enhancement factor can accurately capture the spatial variations in flow over the ice shelf. For flow-line studies of idealised grounded flow over a bumpy topography or a sticky base

10 – both scenarios dominated at depth by bed-parallel shear – the differences between simulated velocities using ESTAR and the Glen flow relation vary according to the value of the enhancement factor used to calibrate the Glen flow relation. These results demonstrate the importance of describing the anisotropic rheology of ice in a physically realistic manner, and have implications for simulations of ice sheet evolution used to reconstruct paleo-ice sheet extent and predict future ice sheet contributions to sea level.

1 Introduction

15 An essential component of an ice sheet model is its formulation of ice rheology, which relates deformation rates to applied stresses. Data from laboratory ice deformation experiments can be used to define flow relations suitable for implementation in numerical ice sheet models. Previous experiments have demonstrated that under conditions of constant stress and temperature, polycrystalline ice with a statistically random distribution of crystallographic c-axes (fabric) initially behaves as a mechanically

20 isotropic material (Budd and Jacka, 1989). We use the term fabric to describe the distribution of crystallographic c-axis orientations within a polycrystalline aggregate. At the commencement of deformation, during the primary stage of creep, the initially high strain rate rapidly decreases. A minimum strain rate is reached during secondary creep (Fig. 1), which is associated with a transitory balance between strain hardening and the strain-induced activation of microstructural recovery processes. With continued strain, a tertiary stage of creep is established (typically observed at strain of $\sim 10\%$ in laboratory experiments), which

is characterised by a dynamic balance between microdeformation and recovery processes, statistically steady-state anisotropic polycrystalline microstructures (e.g., crystal orientation fabric and grain size), and steady strain rates that are enhanced relative to the rate observed during secondary creep.

Tertiary creep, with the associated development of polycrystalline anisotropy driven by the microstructural response to applied stresses, is the predominant mode of ice deformation in ice sheets. The fabric anisotropy and the tertiary strain rates depend on the nature of the applied stresses (Fig. 1).

The prevailing description of ice rheology used in large-scale ice sheet models, the Glen flow relation (Glen, 1952, 1953, 1955, 1958; Nye, 1953), is a creep power law:

$$\dot{\boldsymbol{\varepsilon}} = A(T')\tau_e^{n-1}\boldsymbol{\sigma}', \tag{1}$$

where $\dot{\boldsymbol{\varepsilon}}$ is the strain rate tensor (s^{-1}), τ_e is the effective stress (Pa), proportional to the second invariant of the deviatoric stress tensor $\boldsymbol{\sigma}'$, and n is a power law stress exponent (observations support a value of $n = 3$). $A(T')$ is a temperature dependent flow parameter ($\text{Pa}^{-n}\ \text{s}^{-1}$), for which various parameterisations exist based on laboratory tests and field measurements (e.g., Budd and Jacka, 1989; Cuffey and Paterson, 2010).

The Glen flow relation was empirically derived from secondary creep rates, determined under various conditions of constant stress and temperature, for polycrystalline ice with an initially random distribution of c-axes and assuming mechanical isotropy. While the Glen flow relation captures the observed nonlinear response of ice deformation to an applied stress, it is unable to account for the mechanical anisotropy of polycrystalline ice during tertiary creep (e.g., Nye, 1953; Glen, 1958; Budd et al., 2013). That is, it cannot explain the dependence of tertiary strain rates on the character of the applied stress. To account for the increased deformability associated with tertiary creep, a common adaptation of the Glen flow relation is the inclusion of a constant flow enhancement factor, E_G,

$$\dot{\boldsymbol{\varepsilon}} = E_G A(T')\tau_e^{n-1}\boldsymbol{\sigma}'. \tag{2}$$

The specification of E_G is typically ad hoc: E_G may be selected from reported experimental values (e.g., Duval, 1981; Jacka and Maccagnan, 1984; Pimienta et al., 1987; Treverrow et al., 2012), or used as a model tuning parameter (e.g., to alter the relative contribution of viscous deformation and basal sliding to the overall dynamics of an ice sheet). In either case, a value of E_G that does not vary spatially in connection with the fabric and flow configuration, will lead to an unrealistic spatial distribution of strain rates (Treverrow et al., 2015). Previous studies have used anisotropic flow models or approximations to assign regional values to E_G (e.g., Ma et al., 2010) that may also vary according to the prevailing stress regime.

Budd et al. (2013) recently proposed an anisotropic flow relation based on results from laboratory ice deformation experiments in simple shear, compression, and combinations of these. As tertiary creep rates and the corresponding compatible fabrics were found to vary according to the relative proportions of the simple shear and compression stresses, Budd et al. (2013) defined an enhancement factor E as an anisotropic function of the stress configuration, with separate, experimentally-determined enhancement factors for simple shear-alone and compression-alone. We refer to the generalised form of the anisotropic flow relation proposed by Budd et al. (2013) as ESTAR (Empirical, Scalar, Tertiary, Anisotropic Rheology), since it is based on ter-

tiary (steady-state) creep rates and features a scalar (collinear) relationship between the strain rate and deviatoric stress tensor components.

Here, we describe how to implement ESTAR in large-scale ice sheet models and apply the required changes to the Ice Sheet System Model (ISSM; Larour et al., 2012). ISSM is a thermomechanical finite element model that solves the full system of 5 Stokes equations to describe ice flow. We examine the effect of anisotropy in simple, idealised scenarios of a floating ice shelf and of grounded ice sheets, comparing simulated flow fields using ESTAR with the corresponding isotropic flow modelled by the Glen flow relation. Section 2 presents an overview of anisotropic rheologies, including the experimental and theoretical basis for ESTAR. Section 3 details the implementation of ESTAR in ISSM and its verification against an analytical solution. In Sect. 5, we compare simulations of ice flow with ESTAR and the Glen flow relation using a suite of idealised flow geometries, 10 including selected experiments from the Ice Sheet Model Intercomparison Project for Higher Order Models (ISMIP-HOM; Pattyn et al., 2007).

2 Anisotropic ice rheology

A range of ice rheologies have been proposed to account for polycrystalline anisotropy. They can be broadly grouped in two categories: (1) those defined at the individual ice crystal scale, where the effects of anisotropy are parameterised based on 15 specific properties of individual crystals, and (2) those that describe anisotropic aspects of deformation empirically: either based on regional expectations about local crystallographic microstructure, or through an empirical function of the stress configuration. In this section, we briefly review these two approaches, and the underlying experimental and modelling basis for ESTAR. In what follows, we distinguish between the Glen enhancement factor E_G and the ESTAR enhancement factor $E(\lambda_S)$, which is a function of compression deviatoric and simple shear stresses, parameterised by the shear fraction λ_S. Where 20 necessary, we denote a more general enhancement factor, i.e., with unspecified form, as E.

2.1 Microstructure approaches

Experiments on single crystals of ice demonstrate that deformation occurs predominantly by slip on the crystallographic basal plane, with the yield stress being geometrically related to the magnitude of the applied stress resolved onto the basal plane (Trickett et al., 2000) according to Schmid's Law (Schmid and Boas, 1950). This observation, in conjunction with the develop- 25 ment of crystallographic preferred orientations during deformation of polycrystalline ice to high strains (e.g. Russell-Head and Budd, 1979; Jacka and Maccagnan, 1984; Pimienta et al., 1987; Morgan et al., 1998; DiPrinzio et al., 2005; Durand et al., 2009; Budd et al., 2013; Montagnat et al., 2014), has driven the development of rheological descriptions in which the connection between deviatoric stresses and resulting strain-rates is regarded as an intrinsic material property determined by the effects of microstructure on bulk deformation processes, (e.g. Lile, 1978; Lliboutry, 1993; Azuma and Goto-Azuma, 1996; Staroszczyk 30 and Gagliardini, 1999; Thorsteinsson, 2001; Gödert, 2003; Gillet-Chaulet et al., 2005; Pettit et al., 2007; Placidi et al., 2010). See also the review by Gagliardini et al. (2009). In broad terms, the anisotropic nature of these rheological descriptions is

derived from the geometric relationship between the crystallographic c-axis and the stresses driving deformation, with the role of misorientation relationships between nearest neighbour grains explicitly considered in some cases.

The complexity of numerical flow relations varies according to the extent to which a physically realistic description of microdeformation and recovery processes, or a parameterisation of these, enters into the relationship between strain rates and the stresses driving deformation. Many of these rheological models are more complicated than a collinear flow relation and involve a tensor coupling in place of Eq. 2. A further consideration is the quantitative description of fabric that is used in flow relations. Those incorporating a discrete, c-axis vector based description of fabric (e.g. Lile, 1978; van der Veen and Whillans, 1994; Azuma and Goto-Azuma, 1996; Thorsteinsson, 2002) are only appropriate for highly localised studies and are incompatible with large-scale ice sheet modelling. Flow relations based on a continuous description of fabric, e.g., a parameterised orientation distribution function (ODF) or c-axis orientation tensor are also possible (e.g. Staroszczyk and Gagliardini, 1999; Gödert, 2003; Gillet-Chaulet et al., 2005; Pettit et al., 2007; Placidi et al., 2010). Including any fabric-based rheological description in an ice sheet model requires a separate set of equations governing the fabric evolution. A drawback to such an approach is the computational overhead and uncertainty associated with defining the spatial distribution of fabric within ice sheets, which is poorly constrained by observations. Furthermore, for simplicity, restricted forms of the ODF or orientation tensor are specified, which may not adequately describe all fabrics likely to be encountered in an ice sheet. As such, flow relations utilising a fabric description that relies on fabric evolution equations or that is imposed as a function of location within the ice sheet are currently restricted to regional simulations (e.g., Seddik et al., 2011; Martín and Gudmundsson, 2012; Zwinger et al., 2014).

2.2 Empirical approaches

A second approach comprising: experimental and observational approaches (Li et al., 1996; Wang et al., 2002a, b), modelling (Wang and Warner, 1998, 1999; Hulbe et al., 2003; Wang et al., 2003, 2004; Breuer et al., 2006; Wang et al., 2012), and theoretical studies (Warner et al., 1999), has focussed on the development and assessment of an anisotropic flow relation for polycrystalline ice in which the nature of the crystal fabric and the magnitude of strain rate enhancement, E, are both determined by the stress regime. Specifically, this approach regards the fabric and the enhancement as determined by the relative proportions of the simple shear and normal deviatoric stresses. For such flow relations, it is typically assumed that the spatial variation in dynamic conditions (e.g., flow configuration and temperature) only occur gradually in an ice sheet, so that the microstructure evolves to maintain compatibility with these conditions. That is, throughout an ice sheet the rate of microstructural evolution generally exceeds the rate at which the flow configuration varies. This assumption is supported by experimental observations for pure polycrystalline ice, which demonstrate that an accumulated strain of $\lesssim 10\%$ is required for the microstructure to evolve to a state that is compatible with the flow configuration, irrespective of its initial condition (Jacka and Maccagnan, 1984; Gao and Jacka, 1987; Li and Jacka, 1998; Treverrow et al., 2012).

The anisotropic flow relation proposed by Budd et al. (2013) represents a continuation of this strand. They found that a scalar anisotropic flow relation, i.e., one maintaining the collinear relationship between the components of $\dot{\varepsilon}$ and σ' (τ_e is a scalar function of the second invariant of σ') provides a good fit to laboratory data from combined compression and shear

experiments. Such a scalar anisotropic rheology also simplifies the requirements for implementation within ice sheet models that are already compatible with the (scalar) Glen rheological description. Budd et al. (2013) proposed ESTAR as a suitable candidate scalar anisotropic rheology generalised to arbitrary stress configurations (i.e., not restricted in its application to the limited set of experimental stress configurations described in Li et al. (1996) and Budd et al. (2013)). A simplified version of

5   ESTAR, called ESTAR-MFL (MFL: Minimal Flow Law), has also been incorporated into the ice sheet model SICOPOLIS (SImulation COde for POlythermal Ice Sheets, http://www.sicopolis.net; Greve and Blatter, 2009, 2016).

2.3 Empirical scalar tertiary anisotropic rheology (ESTAR)

Here, we summarise the anisotropic rheology proposed by Budd et al. (2013) – ESTAR – that we are implementing in ISSM as an alternative to the Glen flow relation, to provide a relation more applicable to the tertiary creep of anisotropic polycrystalline

10   ice typical of ice sheets and glaciers. ESTAR is a scalar power law formulation based on tertiary creep rates measured in laboratory ice deformation experiments under various combinations of simple shear and compression that has been generalised to arbitrary stress configurations. Recasting Eqs. 62 and 63 of Budd et al. (2013) to more closely resemble Eq. 2. ESTAR is given by the following expression:

$$\dot{\varepsilon} = E(\lambda_S)A(T')\tau_e^2\boldsymbol{\sigma'}. \tag{3}$$

15   Assuming $n = 3$ in Eq. 2. Eq. 3 only differs from the Glen flow relation by the form of the functional enhancement factor $E(\lambda_S)$, which explicitly depends on the nature of the applied stresses via the shear fraction, λ_S. We note that in contrast to ISSM, flow relations in Budd et al. (2013) are couched in terms of the octahedral shear stress, $\tau_o = \sqrt{2/3}\tau_e$, which provides a more physically meaningful scalar measure of the overall stress magnitude than τ_e (Jaeger, 1969).

$E(\lambda_S)$ in Eq. 3 is defined as

20   $$E(\lambda_S) = E_C + (E_S - E_C)\lambda_S^2, \tag{4}$$

where E_C is a compression enhancement factor, E_S is a simple shear enhancement factor, and λ_S is a non-dimensional variable that takes values in $[0, 1]$. The shear fraction characterises the contribution of simple shear ($\boldsymbol{\tau'}$) to the effective stress (τ_e)

$$\lambda_S = \frac{\|\boldsymbol{\tau'}\|}{\tau_e}. \tag{5}$$

Accordingly, determining the portion of the overall deformation stress that can be regarded as simple shear is the main

25   ingredient in implementing ESTAR. This involves the identification of a particular local plane – the local non-rotating shear plane – and the determination of the shear acting on that plane, $\boldsymbol{\tau'}$, as the measure of simple shear. As discussed in Budd et al. (2013), the importance of moving beyond strain rates to consider other aspects of flow – the 'movement picture' – has been recognised since at least the 1970s (e.g., Budd, 1972; Kamb, 1973; Duval, 1981). Duval (1981) identified the plane normal to the velocity gradient in a simple shear regime as the 'permanent shear plane' and discussed its role in the evolution of crystal

30   fabrics. Budd et al. (2013) proposed a definition for this local plane in an arbitrary flow as the plane containing the vorticity vector associated solely with deformation and the velocity vector. As discussed below they also prescribed a further projection

to remove any component of τ′ parallel to the deformational vorticity
2017-05-05
10.5194/tc-2017-54
journal article
en

to remove any component of $\boldsymbol{\tau}'$ parallel to the deformational vorticity. The collinear nature of ESTAR (Eq. 3) allows λ_S to be written in terms of the corresponding strain rates, which is more convenient for Stokes flow modelling, as

$$\lambda_S = \frac{\dot{\varepsilon}'}{\dot{\varepsilon}_e},\tag{6}$$

where $\dot{\varepsilon}'$ is the magnitude of the shear strain rate on the locally non-rotating shear plane, as defined in Eq. 7 below. In compression-alone scenarios, including three-dimensional uniaxial compression and two-dimensional plane compression and extension, $\lambda_S = 0$, so that $E(\lambda_S) = E_C$. Similarly, for simple shear alone, $\lambda_S = 1$ and $E(\lambda_S) = E_S$.

Analysis of tertiary creep rates for experiments conducted in simple shear-alone and compression-alone suggests that a suitable ratio of E_S to E_C for ice sheets is $\sim 8/3$ (Treverrow et al., 2012). The same data also suggest that $E \propto \sqrt{\tau_e}$ for tertiary creep rates determined over a range of stress magnitudes. A flow relation incorporating stress dependent enhancement could be achieved by employing a creep power-law stress exponent of $n = 3.5$, rather than the more commonly used $n = 3$, assuming both E_S and E_C are described by functions of $\sqrt{\tau_e}$. For simplicity, we have excluded the apparent stress dependence of E_S and E_C in our initial implementation of ESTAR in ISSM since further work is required to verify the stress dependence of E_S and E_C experimentally for complex, combined stress configurations. Accordingly, we use scalar enhancement factors of $E_S = 8$ and $E_C = 3$ for the idealised scenarios examined in this study. These values may be at the higher end of the anticipated range in E_S and E_C for an ice sheet (see e.g., Russell-Head and Budd, 1979). However, the strength of anisotropy and its influence on ice dynamics in comparison to the enhanced Glen flow relation depends on the ratio E_S/E_C and its spatial variation, i.e., the dynamically controlled distribution of $E(\lambda_S)$.

If the enhancement parameters are selected so that $E_C = E_S = E_G$, where E_G is the Glen enhancement factor, ESTAR becomes isotropic and equivalent to the Glen flow relation since $E(\lambda_S) \equiv E_G$. However, the viscous creep behaviour of polycrystalline ice is highly anisotropic and regional variations in the relative proportions of shear and normal strain rates, which are driven by variations in the distribution of the stresses responsible for deformation, mean that spatial contrasts in anisotropy are common and widespread in ice sheets. For this reason, a spatially varying enhancement factor is required for ice sheet modelling (e.g., Morgan et al., 1998; Wang et al., 2002a).

Comparisons of simulations of ice sheet dynamics using ESTAR and the Glen flow relation will be influenced by: the choice of the Glen enhancement parameter, E_G; E_C; E_S; and the spatial distribution of λ_S. The most significant differences between Glen- and ESTAR-based simulations are expected where there are regional contrasts in λ_S. Specific regions where these conditions are likely to arise include: the lateral margins of embayed ice shelves and ice streams; locations where there are changes in dynamic conditions at the bed, e.g., at the transition between bed-parallel shear and basal sliding; ice shelf grounding zones; and where there is significant relief in the bedrock topography. A caveat is that as stated earlier, for ESTAR the assumptions of crystallography and deformation rates being compatible with the instantaneous stress/deformation regime requires that this does not change too rapidly along the flow.

3 Implementation of ESTAR

The magnitude of the shear strain rate defined on the local non-rotating shear plane, $\dot{\varepsilon}'$ from Eq. 6, is central to the formulation of ESTAR. The full prescription, following Budd et al. (2013), involves the following expression

$$\dot{\varepsilon}' = \|\dot{\boldsymbol{\varepsilon}} \cdot \mathbf{n} - (\mathbf{n} \cdot (\dot{\boldsymbol{\varepsilon}} \cdot \mathbf{n}))\,\mathbf{n} - (\hat{\boldsymbol{\omega}}_D \cdot (\dot{\boldsymbol{\varepsilon}} \cdot \mathbf{n}))\,\hat{\boldsymbol{\omega}}_D\|, \qquad (7)$$

where: $\mathbf{n}$ is the unit normal to the non-rotating shear plane, $\hat{\boldsymbol{\omega}}_D$ is the unit vector parallel to that part of the vorticity that is associated solely with deformation, and $\dot{\boldsymbol{\varepsilon}}$ is the strain rate tensor. The unit normal to the non-rotating shear plane $\mathbf{n}$ is defined as the normalised cross product of the velocity and the deformational vorticity

$$\mathbf{n} = \frac{\mathbf{v} \times \boldsymbol{\omega}_D}{\|\mathbf{v} \times \boldsymbol{\omega}_D\|}. \qquad (8)$$

The last projection term in Eq. 7 was proposed in Budd et al. (2013) to prevent any shear component parallel to the deformational vorticity from contributing to the measure of simple shear.

The vorticity of a flow, whether viewed as the anti-symmetrised part of the velocity gradient tensor or as the usual vector $\boldsymbol{\omega} = \nabla \times \mathbf{v}$, contains motions associated with both deformation and local rigid-body rotation. The locally non-rotating shear plane is intended to be rotating with any rigid rotation portion of the flow field, so it is only vorticity associated with the deformation process that is relevant to determining the shear fraction. Accordingly we decompose vorticity into deformational and rotational parts:

$$\boldsymbol{\omega} = \nabla \times \mathbf{v} = \boldsymbol{\omega}_D + \boldsymbol{\omega}_R. \qquad (9)$$

For the present implementation it is convenient to decompose the vorticity further, into vectors perpendicular and parallel to the velocity direction as follows:

$$\boldsymbol{\omega} = \boldsymbol{\omega}_D^{\perp} + \boldsymbol{\omega}_R^{\perp} + \boldsymbol{\omega}_D^{\parallel} + \boldsymbol{\omega}_R^{\parallel}. \qquad (10)$$

From Eq. 8, only the perpendicular projection $\boldsymbol{\omega}_D^{\perp}$ of the deformational vorticity is relevant in determining the direction of the normal to the non-rotating shear plane. This is fortunate since the perpendicular projection of the rotational vorticity can be calculated directly for steady flow from the flow speed and curvature of the local flowline, and is oriented along the bi-normal to the flow-line. The decomposition of the component of vorticity parallel to the flow direction, conventionally termed swirling motion, into deformational and rotational pieces is not so straightforward, but we can use the following expression, which can be calculated using variables available within an individual element of ISSM to generate a vector suitable for computing $\mathbf{n}$:

$$\tilde{\boldsymbol{\omega}}_D = \nabla \times \mathbf{v} - \frac{2\mathbf{v} \times ((\mathbf{v} \cdot \nabla)\mathbf{v})}{\|\mathbf{v}\|^2}. \qquad (11)$$

This vector contains the correct perpendicular component $\boldsymbol{\omega}_D^{\perp}$ to compute $\mathbf{n}$ using Eq. 8, but contains all of $\boldsymbol{\omega}_D^{\parallel} + \boldsymbol{\omega}_R^{\parallel}$. We can obviously also project out the component parallel to velocity to find

$$\boldsymbol{\omega}_D^{\perp} = \tilde{\boldsymbol{\omega}}_D - (\mathbf{v} \cdot \tilde{\boldsymbol{\omega}}_D)\frac{\mathbf{v}}{\|\mathbf{v}\|^2}. \qquad (12)$$

In the present implementation of ESTAR, we assume that swirling effects are small for flows with the relevant spatial scales, aspect ratios etc., which can be verified from the modelled flow-fields, and hence $\boldsymbol{\omega}_D^{\parallel}$ is also expected to be small. We use the unit vector corresponding to $\boldsymbol{\omega}_D^{\perp}$ (i.e., $\hat{\boldsymbol{\omega}}_D$) in Eq. 7 for our computation of $\dot{\varepsilon}'$. This corresponds to extracting the component of the shear resolved on the non-rotating shear plane which is parallel to the velocity direction, which could be regarded as an alternative generalisation for the simple shear to that proposed by Budd et al. (2013). No approximation is involved for flows that are exactly two dimensional in character, since vorticity is always orthogonal to velocity in such situations.

4 Analytical verification

We perform convergence tests in order to verify the ISSM implementation of ESTAR within the full Stokes (FS) and higher order (HO) models. The objective of these tests is to compare the model results to analytical solutions for different mesh resolutions. As the mesh becomes finer, the error between the model and the analytical solution (i.e., $\sqrt{\int_\Omega (X - X_a)^2 / \int_\Omega X_a^2}$, for model solution X, analytical solution X_a, and domain Ω) should decrease, with a cubic dependence on resolution for FS (quadratic for ice pressure) when using Taylor-Hood finite elements, and a quadratic dependence for HO using P1×P1 finite elements (e.g., Ern and Guermond, 2004).

We designed our analytical solutions by considering a three-dimensional, grounded, isothermal ice slab of unit dimension lying on a flat bed topography, with cartesian coordinates (x, y, z), where z is vertically upward and where there is no gravitational force. The FS three-dimensional velocity field is given by

$$v_x(x, y, z) = 3z, \tag{13}$$
$$v_y(x, y, z) = 2x + y, \tag{14}$$
$$v_z(x, y, z) = -z, \tag{15}$$

and the HO velocity field by

$$v_x(x, y, z) = x^2, \tag{16}$$
$$v_y(x, y, z) = 3z + y. \tag{17}$$

In the case of the HO model, $v_z(x, y, z)$ is recovered by incompressibility. For both FS and HO models, we use ESTAR shear and compression enhancement factors of $E_S = 3$ and $E_C = 1$, and the flow parameter $A(T') = 2/3 \, \text{Pa}^{-3} \, \text{s}^{-1}$. The open source mathematics software system SageMath (http://www.sagemath.org/) is used to calculate analytical solutions for the force balance equations based on the above velocity fields:

$$f_x(x, y, z) = -\left(\frac{\partial \sigma'_{xx}}{\partial x} + \frac{\partial \sigma_{xy}}{\partial y} + \frac{\partial \sigma_{xz}}{\partial z} \right), \tag{18}$$
$$f_y(x, y, z) = -\left(\frac{\partial \sigma_{xy}}{\partial x} + \frac{\partial \sigma'_{yy}}{\partial y} + \frac{\partial \sigma_{yz}}{\partial z} \right), \tag{19}$$
$$f_z(x, y, z) = -\left(\frac{\partial \sigma_{xz}}{\partial x} + \frac{\partial \sigma_{yz}}{\partial y} + \frac{\partial \sigma'_{zz}}{\partial z} \right). \tag{20}$$

Here, the deviatoric stress fields are calculated using ESTAR specified in Eq. 3. When the total, rather than deformation, vorticity (i.e., without inclusion of the rigid body correction or removal of the vorticity component aligned with the flow) is used in the calculation of ESTAR, the FS analytical solution for (f_x, f_y, f_z) comprises (20 521, 9 190, 20 523) characters. By contrast, non-trivial analytical solutions for the forcing functions that are calculated from an anisotropic enhancement factor that is based on the deformation, rather than total, vorticity are at minimum 200 000 characters, well in excess of the character limits for most compilers. Hence, we verify ESTAR using the total, rather than the deformational, vorticity.

To test the numerical implementation of ESTAR, ISSM is forced using the analytical expressions for f_x, f_y, and f_z in Eqs. 18-20 and the resulting three-dimensional flow field is compared with the relevant analytical specification in Eqs. 13-17. Since the aim is to verify correct coding of the ESTAR modifications within ISSM, we apply the analytic velocities on the faces as the boundary conditions. Four sets of element sizes are used for each of the FS and HO models, increasing in resolution from 0.2 (272 elements over 5 vertical layers) to 0.08 (4656 elements over 13 vertical layers). We find convergence powers of 2.5 (v_x), 3.1 (v_y), and 2.6 (v_z) for FS, respectively, and 1.4 (v_x) and 1.1 (v_y) for HO (Fig. 2), which are consistent with theory and verify our implementation.

5 Application of ESTAR to idealised scenarios

ESTAR was applied to a suite of test cases. The first case we present simulates flow in an embayed ice shelf; the second two are based on experiments from the Ice Sheet Model Intercomparison Project for Higher Order Models (ISMIP-HOM; Pattyn et al., 2007). The ISMIP-HOM experiments describe idealised scenarios of ice flow where the bed topography or basal friction vary. ISSM has already been validated against each of these experiments (Larour et al., 2012).

In each experiment, the velocity, surface, and thickness fields were allowed to run to steady-state, as defined in each section (the original ISMIP-HOM experiments were simply diagnostic). The ice sheet is isothermal in each case.

As mentioned in the previous section, we use ESTAR shear and compression enhancement factors of $E_S = 8$ and $E_C = 3$, respectively (Treverrow et al., 2012). For each experiment, we perform simulations using Glen enhancement factors of 1, 3, 5, and 8; this range of enhancement factors facilitates a 1:1 comparison with ESTAR for different governing stress regimes, yet remains consistent with the broad range of enhancement factors used in previous ice sheet model experiments (e.g., Greve, 1997; Parizek and Alley, 2004; Tarasov and Peltier, 2004; Martin et al., 2011). The ISMIP-HOM experiments used the same parameter values (Pattyn et al., 2007) unless otherwise indicated.

5.1 Flow through an embayed ice shelf

The first experiment simulates three-dimensional flow through a rectangular embayed ice shelf. The experiment was carried out for model domains with transverse spans $x \in [0, L]$, for $L = 20, 60$, and 100 km and along-flow dimension $y \in [0, 100]$ km. The initial ice thickness decreases uniformly from 1000 m at the grounded zone to 300, 600, and 850 m at the ice front for the $L = 20, 60$, and 100 km cases, respectively. The main features of the anisotropic effects are similar regardless of aspect ratio, so we focus our discussion on one transverse length scale: $L = 20$ km. The plan view mesh is extruded ten quadratically-spaced

layers in the vertical. A no-slip boundary condition is applied along the $x = 0$ and $x = L$ km side boundaries. At the inflow boundary, the y-component of velocity is set to

$$v_y(x,0) = V_0 e^{-\left[\frac{5(x - x_{\mathrm{mid}})}{2L}\right]^8}, \tag{21}$$

where $V_0 = 100$ m yr^{-1} and $x_{\mathrm{mid}} = L/2$. As is standard, ocean water pressure is applied at the ice-ocean interface where

5 tangential (traction) stresses vanish. It is assumed that there is no surface or basal melting or accumulation over the ice shelf domain. The flow parameter $A(T') = 1.74 \times 10^{-25}$ Pa^{-3} s^{-1}, is set using the Budd and Jacka (1989) value for an isothermal ice shelf of $-20\,°C$.

We run the HO ice flow model for each of the ESTAR and Glen rheologies to steady-state, which we define to be reached when the mean velocity change over the surface mesh points is less than 1×10^{-2} m yr^{-1} between two consecutive time steps

10 (of $\triangle t = 2$ yr). ISSM uses the Blatter-Pattyn form of the HO approximation (Blatter, 1995; Pattyn, 2003), which assumes that horizontal gradients in the vertical velocities are negligible compared with vertical gradients in the horizontal velocities when computing vertical shear, and longitudinal derivatives of vertical shear stress (bridging effects) are ignored.

The Glen and ESTAR HO steady-state surface velocity magnitudes are compared in Fig. 3, where a Glen enhancement factor of $E_G = 8$ has been used. The patterns of ice flow are similar for the two rheologies: in each case the ice velocity increases

15 as it flows through the ice shelf, reaching its maximum at the ice front. Over most of the domain the velocities are in close agreement, reflecting the dominance of the shear flow. However, the Glen velocities are up to 17% larger than the ESTAR velocities at the ice front, where the flow field is predominantly extensive in accordance with the ice front boundary conditions. The differences in velocities can be attributed to differences in flow enhancement factors for simple shear and compression. In the centre of the ice shelf and across the ice front, where longitudinal and vertical normal stresses dominate, the Glen

20 enhancement is as much as $8/3$ times larger than the corresponding ESTAR enhancement.

The steady-state thickness ratio for the two rheologies is shown in Fig. 3d. In both cases, the equilibrated ice shelf is thicker along the centre line and thinner towards the side margins where ice flow is slower, and thicknesses agree within 5% over much of the domain. However, the Glen ice shelf is consistently thinner than the ESTAR ice shelf, particularly along the centre line where Glen velocity is enhanced relative to ESTAR, and it is up to 20% thinner at the ice front. Reducing the Glen

25 enhancement factor (i.e., for $E_G = 1, 3, 5$) results in almost identical steady-state velocities to the $E_G = 8$ case. However, the ice shelf thicknesses for $E_G = 1, 3, 5$ are then uniformly greater across the shelf than the $E_G = 8$ case by approximately 100%, 40%, and 17%, respectively.

The ESTAR strain rate components are presented in Fig. 4. As expected, shear strain rate in the $x - y$ plane is very high near the lateral boundaries (Fig. 4d). However, it dominates the effective strain rate (and hence λ_S) well beyond those margins

30 (Fig. 5), before decreasing towards the centre line, where it identically vanishes. Towards the ice-ocean front, each of the normal strain rates $- \dot{\varepsilon}_{xx}$, $\dot{\varepsilon}_{yy}$, and $\dot{\varepsilon}_{zz}$ – increase in magnitude, reaching their maxima at the front. The (approximately) longitudinal $\dot{\varepsilon}_{yy}$ is the dominant normal strain rate component and is extensive towards the front. Due to the confined geometry, towards the front $\dot{\varepsilon}_{yy}$ is largely balanced by $\dot{\varepsilon}_{zz}$, which drives ice shelf thinning. Transverse normal strain rate $\dot{\varepsilon}_{xx}$ plays a lesser role at the ice-ocean front than the remaining normal strain rates. It is extensive along the front as the streamlines diverge,

but changes sign to compressive towards the corners. The patterns in the component strain rates, including the dominance of vertical compression strain rates in the centre of the ice shelf and at the ice-ocean front, are evident in the strain rate on the non-rotating shear plane (NRSP strain rate) and the effective strain rate ($\dot{\varepsilon}_e$; Fig. 5), the ratio of which sets the magnitude of λ_S. In the ESTAR embayed ice shelf simulation, the vanishing of basal traction and the depth independent nature of the inflow

5   velocity lead to an almost 2D flow field with local non-rotating shear planes essentially vertical where they can be defined – there being neither $x - y$ plane shear nor vorticity along the centre line. We note that $\dot{\varepsilon}_{yy}$ decreases in magnitude with depth at the ice-ocean front, coincident with ice front tilting (Weertman, 1957), which also gives rise to some local shear deformation in the $y - z$ plane.

The FS ice flow model was computed for 1 year (i.e., steady state had not yet been reached) and the results compared with

10   the HO simulation results for the same model period (results not shown). At the ice front, the HO velocities are everywhere within 5% of the FS velocities, with the maximum differences occurring near the lateral boundaries. Across the shelf, the HO component velocities accord well with the FS velocities. The magnitude and spatial patterns of $\dot{\varepsilon}'$, $\dot{\varepsilon}_e$, and λ_S also agree well between the two flow equations.

Computation times for FS simulations using each of the two rheologies, and for increasing mesh resolutions, are summarised

15   in Table 1. In each case, the model was run for 1 month with a time step of $\triangle t = 1 \times 10^{-4}$ yr. The ESTAR simulation computation times are no more than 3% slower than the corresponding Glen times, and the simulation times for the two rheologies converge as the mesh resolution increases. This result gives us confidence that ESTAR is essentially as computationally-efficient as the Glen rheology.

5.2   ISMIP-HOM experiment B: two-dimensional flow over a bumpy bed

20   ISMIP-HOM Experiment B (ISMIPB) describes two-dimensional flow (x horizontal, z vertical) over a bed topography that varies sinusoidally, according to the following equation

$$z_b(x) = z_s(x) - 1000 + 500 \sin\left(\frac{2\pi x}{L}\right). \tag{22}$$

where $z_s(x) = -x \tan\alpha$, for a mean bed slope of $\alpha = 0.5°$, and L controls the scale of the bedrock undulation. We take $z_s(x)$ as the initial surface so that the mean initial ice thickness is 1000 m. As for the embayed ice shelf experiment, we discuss

25   only the $L = 20$ km case since the anisotropic effects are similar regardless of aspect ratio. The flow parameter is fixed at 3.96×10^{-25} Pa^{-3} s^{-1}, corresponding to an ice temperature of approximately $-14°$ C (Budd and Jacka, 1989). The value for the flow parameter in the original ISMIPB was 3.17×10^{-24} Pa^{-3} s^{-1}, which corresponds to a Budd and Jacka (1989) ice temperature of approximately $-3.6°$ C. We have reduced the original flow parameter by a factor of 8 (i.e., equal to E_S) to ensure our results are as close as possible to the original ISMIP-HOM experiments. Periodic boundary conditions are applied

30   at the vertical edges of the domain and a no-slip boundary condition is applied at the base. In this and the following two-dimensional test case, the normal to the non-rotating shear plane is simply the direction perpendicular to the velocity and there is no uncertainty about the vorticity (which has only one non-vanishing component) being perpendicular to the velocity.

Steady-state is reached when the mean velocity change over the surface mesh points is less than 1×10^{-2} m yr^{-1} between two consecutive time steps of $\triangle t = 1$ yr for this and the following ISMIP-HOM experiment.

The ESTAR and Glen FS steady-state along-flow velocities (v_x) are compared in Fig. 6 and the shear fraction used to calculate the ESTAR enhancement is shown in Fig. 7a. When $E_G = E_S = 8$, the ESTAR velocities are marginally slower than the Glen velocities throughout the domain, regionally by as much as 6%. Although, we note that in a real-world situation, a local difference of 6% may not be significant to overall flow. One major contrast occurs either side of the topographic bump in the near-surface layers (Fig. 6c) where normal stresses dominate ($\lambda_S < 1$) and E_G is greater than E_C (Fig. 7). This reduces the shear deformation in the upper-layers for ESTAR compared to Glen, leading to slightly lower horizontal velocities. Another velocity contrast occurs directly above the topographic depression. Since deformation here is clearly shear dominated ($\lambda_S = 1$; Fig. 7), the difference must arise from a lower shear stress in the ESTAR case, reflecting indirectly the stiffer ice in the upper layers because $E(\lambda_S) < E_G = 8$.

Figure 7 also shows the FS shear and normal strain rates for the ESTAR simulation. The dominance of high values of λ_S indicates that bed-parallel simple shear is the main driver of ice flow in ISMIPB with the expected transition through the ice column from compression/extension-dominated flow near the surface to shear-dominated flow near the non-slip bed. Note that while our component strain rates are locked into a global cartesian frame, λ_S denotes the relative importance of simple shear on local non-rotating shear planes. High shear peaks appear directly over the topographical bump and depression, extending further into the surface layers than in surrounding regions. The locations of the peaks correspond to transitions between extensive and compressive longitudinal stresses, centred on "transition curves", along which normal strain rates are identically zero at some point. In order to examine the dynamics giving rise to the high shear peaks, we consider the following exact form of λ_S^2 (for this two-dimensional flow field) expressible in the cartesian frame components

$$\lambda_S^2 = \frac{\alpha \dot{\varepsilon}_{xx}^2 + \beta \dot{\varepsilon}_{xz}^2 + \gamma \dot{\varepsilon}_{xx} \dot{\varepsilon}_{xz}}{\dot{\varepsilon}_{xx}^2 + \dot{\varepsilon}_{xz}^2}, \tag{23}$$

for spatially varying coefficients α, β, and γ. Since there is no surface accumulation, local non-rotating shear planes are parallel to the ice sheet surface. The traction free surface boundary condition implies $\lambda_S = 0$ there, except that if $\dot{\varepsilon}_e$ vanishes, λ_S is technically undefined. We set $\lambda_S = 0$ for vanishing $\dot{\varepsilon}'$ in such situations. It is apparent from Eq. 23 that along transition curves, where $\dot{\varepsilon}_{xx} = \dot{\varepsilon}_{zz} = 0$, $\lambda_S^2 = \beta$, independent of (non-zero) $\dot{\varepsilon}_{xz}$ strain rate. We find that $\beta \to (1 - S_x^2)^2$ towards the surface (i.e., for surface slope in the x-direction S_x) along the transition curve, in order to satisfy the surface boundary condition. This indicates that λ_S should be finite along the transition curve all the way to the surface. The fact that $\lambda_S \to 0$ along the transition curves towards the surface in Fig. 7 may also be a consequence of mesh averaging over elements such that there is not necessarily an exact point in our finite mesh for which $\dot{\varepsilon}_{xx}$ is identically equal to 0. Note that away from the transition curves λ_S does go to zero at the surface, associated with vanishing shear on the non-rotating shear plane there.

The FS spatial pattern of velocities is consistent for both ESTAR and Glen using each of the Glen enhancement factors $E_G = 1, 3, 5, 8$. Naturally, the Glen velocities decrease with decreasing enhancement factor (as the ice becomes stiffer): for $E_G = E_C = 3$, the Glen velocity magnitudes are 38-40% of the corresponding ESTAR velocities; for $E_G = 1$, Glen velocities are only 16-17% of the corresponding ESTAR velocities. These results indicate that the velocities in the Glen case scale

exactly with the choice of E_G. This follows from the nature of the boundary conditions here, so that one can rescale velocity to compensate for changes in E_G.

In addition to the ESTAR FS simulation of ISMIPB, we performed an HO simulation to investigate the representation of anisotropic flow in that approximation scheme. Figure 8 compares velocities, shear fractions λ_S, and anisotropic viscosities, and their ratios, between HO and FS simulations. The HO velocities are slower than the FS velocities throughout the domain. Generally, this is attributable to the neglect of strain rate components – notably the horizontal gradient of vertical velocity – in the HO force balance equations, leading to stiffer ice in the HO approximation. The maximum differences between the HO and FS velocities occur in the basal layers. Consistent with Pattyn et al. (2008), in the near-surface layers, HO velocities are everywhere within 3% of the FS velocities, with larger differences between HO and FS velocities directly over the topographic bump and depression. The differences between HO and FS velocities are magnified in the near-surface layers over the topographic bump relative to the topographic depression. In combination with the neglect of strain rate components in the HO approximation, this difference arises due to slight differences in the locations of vanishing longitudinal strain rates. The local viscosity maxima in the near-surface layers also correspond to regions of vanishing longitudinal strain rates. For these locations, the Glen viscosities would be infinite, but are limited to a maximum value in the ISSM implementation.

5.3 ISMIP-HOM experiment D: two-dimensional flow over a sticky spot

ISMIP-HOM experiment D (ISMIPD) describes a two-dimensional domain over which the basal friction coefficient η varies sinusoidally in the horizontal direction. A Paterson-type friction law (Paterson, 1994) of the following form is used

$$\tau_b = -\eta^2 v_b, \tag{24}$$

where τ_b is the basal stress and v_b the basal velocity, and η varies according to the equation

$$\eta^2 = 1000 + 1000 \sin\left(\frac{2\pi}{L}x\right). \tag{25}$$

The bed topography and the initial ice surface are inclined planes with a slope of $0.1°$, and the initial thickness is 1000 m throughout the domain. As before, the flow parameter is $A(T') = 3.96 \times 10^{-25}$ Pa^{-3} s^{-1} (the ISMIPB and ISMIPD original flow parameters were equal). Periodic boundary conditions are applied at the edges of the domain.

First, the Glen and ESTAR FS stress balance (diagnostic) results for ISMIPD are compared (upper panels, Fig. 9). Note that applied stresses from the initial slope are uniform for this solution type. Along-flow velocities (v_x) are lowest over the sticky spot (0-10 km), and greatest over the slippery spot (10-20 km). However, the contribution from the deformation flow is the other way around since there is negligible vertical shear where the basal friction vanishes. The Glen isotropic and ESTAR anisotropic viscosities in the basal layers directly over the sticky spot are approximately equal, but towards the surface the ESTAR ice becomes stiffer over the sticky spot. By contrast, over the slippery spot, the ESTAR ice is on average 1.8 times stiffer than the Glen ice (see λ_S in Fig. 10a), leading to ESTAR velocities that are up to 10% slower there. For the deformation velocities alone, the maximum difference between the ESTAR and Glen velocities occurs over the sticky spot where ESTAR velocities are up to 7% faster (ignoring the region over the slippery spot where both the ESTAR and Glen deformation velocities are identically zero).

We next consider the FS prognostic results for Glen and ESTAR. Over the sticky spot, vertical shear develops, leading to faster velocities in the upper part of the column (Fig. 9d-e). This is required by continuity, given the low basal velocities over the sticky spot, to balance the block flow over the slippery section. Sliding occurs throughout the domain. The basal velocities increase over the interval where the basal friction coefficient decreases, with a corresponding adjustment in the upper layer velocities. This is part of the transition to block flow over the slippery spot.

With a Glen enhancement factor equal to the ESTAR shear enhancement factor, the total Glen FS velocities are everywhere within 1% of the corresponding ESTAR velocities, with the maximum difference occurring in the near-surface layers over the sticky spot (0-5 km), where the ESTAR ice is stiffer (Fig. 10). The component strain rates and shear fraction λ_S are illustrated in Fig. 10. The distribution of λ_S evolves primarily due to the evolution of normal stresses to steady-state. Shear dominates ($\lambda_S > 0.5$) throughout most of the domain (i.e., for values of the basal friction coefficient>10% of the maximum value). In the region of maximum stickiness at approximately 5 km, the shear stresses are greatest, while in the near-surface layers longitudinal stresses develop either side of the sticky spot.

In examining the evolution of the FS strain rates to steady-state, the shear is largely unchanged although a steeper profile develops over the sticky spot, while longitudinal normal strain rates are reduced by about an order of magnitude over most of the domain. Naturally, a compressive to extensive transition occurs across the sticky spot and the transition curves (vanishing normal strain rates) now resemble the ISMIPB case (Fig. 7b) rather than their diagnostic starting point (Fig. 10b). The change in the normal strain rates increases the vertical extent of the shear enhancement (Fig. 10d), except over the slippery spot.

6   Discussion

The ISMIP-HOM experiments B and D simulated scenarios in which the dominant control of flow was bed-parallel simple shear. Only small differences ($< 6\%$ for ISMIPB and $< 1\%$ for ISMIPD) were apparent between the Glen and ESTAR velocities for a Glen enhancement factor equal to the ESTAR shear enhancement factor ($E_G = E_S$). These results suggest that close agreement with the ESTAR results might be achieved more generally by this choice of the Glen enhancement factor. The results provide a physical rationale to replace the ad hoc enhancement factors typically used in grounded ice sheet modelling. Nevertheless, there remain scenarios of ice flow over grounded ice with more complicated stress regimes than those simulated in the ISMIP-HOM experiments presented here (e.g., ice stream flow with similar contrasts in shear dominated margins and normal stress dominated central regions; flow close to rugged bedrock topography where combinations of shear and normal stresses may be important; or, generally, regions in which λ_S demonstrates large spatial variations corresponding to different stress regimes). In these instances, tuning the Glen enhancement factor may not be able to adequately account for multiple, or varying, controls on ice velocities, nor will it necessarily result in a physically realistic enhancement factor.

Our simulations of embayed ice shelf flow comparing ESTAR and isotropic rheology showed that no single Glen enhancement factor (E_G) can approximate the anisotropic flow characteristic of the stress regimes encountered. Our most significant result indicated that for an embayed ice shelf, a choice of $E_G = E_S$ to reproduce the overall velocities, which are controlled by lateral shear, overestimated velocities near the ice front by up to 17%. This is a consequence of excessively soft ice for the Glen

case in the zone near the ice front where extensional normal stresses dominate. The steady-state Glen ice shelf was accordingly up to 20% thinner than the ESTAR ice shelf in this region. These results highlight one of the key failures of the Glen flow relation in adequately accounting for complex, spatially varying stress regimes in its prescription of ice flow. The addition of an enhancement factor E_G to the Glen flow relation provides some compensation for the flow enhancement associated with

5   microstructural development (i.e., rescaling the minimum creep rate data conventionally used in prescribing the Glen flow relation, e.g., table 3.3, Cuffey and Paterson, 2010). However, such a modification does nothing to allow for the anisotropic (stress configuration dependent) aspects of ice rheology that are characteristic of tertiary creep. The improvement offered by ESTAR is that the specification of the pattern and degree of enhancement is physically based, varying spatially as a function of the stress configuration. This is achieved without the complication of detailed treatment of microstructural information. For

10   near-surface regions of the ice sheet, there may be some lag in the development of anisotropy that is not captured by ESTAR. However, in this zone, both stresses and temperatures are low, so the resulting deformation rates are also low. As such, it is unlikely that an over-enhancement in this zone will impact significantly on the overall dynamics of the ice sheet.

Our embayed ice shelf results have significant implications for ice sheet model simulations that rely on the Glen flow relation to simulate past, present, and future ice flow, which are used to constrain uncertainty in reconstructions and projections of sea

15   levels. In particular, the result of unrealistically fast thinning ice, as simulated with the Glen flow relation, is to deform an ice shelf, which could lead to unrealistic ice shelf geometries and affect buttressing if it were to spread beyond the "passive ice" sector (Fürst et al., 2016) near the ice front. Our findings motivate further enquiry into the simulated ice sheet dynamics of glaciers, the flow of which is governed by anisotropy as captured in ESTAR rather than the Glen flow relation.

In order to measure the impact of an anisotropic rheology on simulated ice dynamics, the ISMIP-HOM and embayed ice

20   shelf experiments were carried out assuming isothermal conditions. However, strong vertical gradients in temperature, where they exist, will be a stronger control on viscosity than the factor of $8/3$ in anisotropic enhancement. This is particularly relevant for the ISMIP-HOM experiments simulated here for simple shear dominated flow.

Many large-scale ice sheet model simulations are run using approximations to the full Stokes (FS) equations, notably higher order (HO, e.g., Blatter, 1995; Pattyn, 2003), shelfy-stream (e.g., MacAyeal, 1989; Morland and Zainuddin, 1987), or shallow

25   ice (e.g., Hutter, 1982) approximations. We compared the ESTAR FS simulations for the embayed ice shelf, ISMIPB, and ISMIPD, with corresponding HO simulations. The local differences between the ESTAR FS and HO simulations were typically smaller than the corresponding differences between ESTAR and the Glen rheology. However, we only performed simulations in idealised situations where the approximations underlying the HO flow equations were generally expected to hold. We anticipate more pronounced differences between the FS and HO flow equations in regions where these assumptions fail. The magnitude

30   of such differences will be explored in future studies.

The focus of this study was to explore the effect of a contrast between the predicted dynamic response of an ice sheet to varying proportions of simple shear and normal stresses when using isotropic (Glen) and anisotropic (ESTAR) descriptions of rheology. Our results, particularly with respect to the differences between the Glen and ESTAR simulations, are sensitive to the choice of E_S and E_C. Experimental evidence (Treverrow et al., 2012) suggests that the ratio $E_S/E_C = 8/3$, rather than

35   their overall magnitude, is the dominant control in the level of enhancement $E(\lambda_S)$ and corresponding dynamic response of

grounded and floating ice sheets. Here, we used values of $E_S = 8$ and $E_C = 3$, which are based on laboratory experiments of tertiary creep (Treverrow et al., 2012), and which yield values for the overall enhancement that are compatible with estimates from borehole inclination measurements (e.g., Russell-Head and Budd, 1979) and modelling studies (e.g., Wang and Warner, 1999). Nevertheless, further investigation into suitable values of E_S and E_C to use in numerical modelling studies of grounded
5 and floating ice sheets is warranted.

7 Conclusions

We have investigated anisotropic flow as represented by the empirical, scalar, tertiary, anisotropic rheology ESTAR, in the context of idealised experiments for an embayed ice shelf, and in two-dimensional models of grounded ice flow over bumpy or sticky beds. We have demonstrated that ESTAR is a computationally-efficient anisotropic rheology for large-scale ice sheet
10 models. We have highlighted that ESTAR produces different flow responses compared with the prevailing rheological description based on the Glen flow relation, in regions where simple shear and normal stresses, and combinations of these, are drivers of ice flow. Further investigation into the capabilities of ESTAR to replicate real-world ice sheet flow in Antarctic outlet glaciers is currently underway.

Code availability. The results from this work are reproducible using ISSM (from version 4.11). The current version of ISSM is available for
15 download at https://issm.jpl.nasa.gov. The ISMIP-HOM experiments are documented in Pattyn et al. (2007).

Competing interests. The authors have no competing interests.

Acknowledgements. This work was supported under the Australian Research Council's Special Research Initiative for Antarctic Gateway Partnership (Project ID SR140300001), and the Australian Government's Cooperative Research Centres Programme through the Antarctic Climate and Ecosystems Cooperative Research Centre (ACE CRC). The University of Tasmania supported the visit of MM to Hobart. This
20 research was undertaken with the assistance of resources from the National Computational Infrastructure (NCI), which is supported by the Australian Government.

References

Azuma, N. and Goto-Azuma, K.: An anisotropic flow law for ice sheet ice and its implications, Ann. Glaciol., 23, 202–208, 1996.

Blatter, H.: Velocity And Stress-Fields In Grounded Glaciers: A Simple Algorithm For Including Deviatoric Stress Gradients, J. Glaciol., 41, 333–344, 1995.

5 Breuer, B., Lange, M. A., and Blindow, N.: Sensitivity studies on model modifications to assess the dynamics of a temperature ice cap, such as that on King George Island, Antarctica, J. Glaciol., 52, 235–247, 2006.

Budd, W. and Jacka, T.: A review of ice rheology for ice sheet modelling, Cold Reg. Sci. Technol., 16, 107–144, 1989.

Budd, W. F.: The development of crystal orientation fabrics in moving ice, Z. Gletscherkd. Glazialgeol, 8, 65–105, 1972.

Budd, W. F., Warner, R. C., Jacka, T. H., Li, J., and Treverrow, A.: Ice flow relations for stress and strain-rate components from combined

10   shear and compression laboratory experiments, J. Glaciol., 59, 374–392, doi:10.3189/2013JoG12J106, 2013.

Cuffey, K. and Paterson, W. S. B.: The Physics of Glaciers, 4th Edition, Elsevier, Oxford, 2010.

DiPrinzio, C., Wilen, L., Alley, R., Fitzpatrick, J., Spencer, M., and Gow, A.: Fabric and texture at Siple Dome, Antarctica, J. Glaciol., 51, 281–290, 2005.

Durand, G., Gagliardini, O., Zwinger, T., Le Meur, E., and Hindmarsh, R.: Full Stokes modeling of marine ice sheets: influence of the grid

15   size, Ann. Glaciol., 50, 109–114, 2009.

Duval, P.: Creep and fabrics of polycrystalline ice under shear and compression, J. Glaciol., 27, 129–140, 1981.

Ern, A. and Guermond, J.-L.: Applied Mathematical Sciences, vol. 159, chap. Theory and practice of finite elements, pp. 175–217, Springer, 2004.

Fürst, J. J., Durand, G., Gillet-Chaulet, F., Tavard, L., Rankl, M., Braun, M., and Gagliardini, O.: The safety band of Antarctic ice shelves,

20   Nat. Clim. Change, 6, 479–482, doi:10.1038/NCLIMATE2912, 2016.

Gagliardini, O., Gillet-Chaulet, F., and Montagnat, M.: A review of anisotropic polar ice models: from crystal to ice-sheet flow models, in: Physics of Ice Core Records II, edited by Hondoh, T., pp. 149–166, Institute of Low Temperature Science, Hokkaido University, Sapporo, Japan, 2009.

Gao, X. and Jacka, T.: The approach to similar tertiary creep rates for Antarctic core ice and laboratory prepared ice, Journal de Physique,

25   Colloque C1, supplement to no. 3, Tome 48, pp. 289–296, 1987.

Gillet-Chaulet, F., Gagliardini, O., Meyssonnier, J., Montagnat, M., and Castelnau, O.: A user-friendly anisotropic flow law for ice-sheet modelling, J. Glaciol., 51, 3–14, doi:10.3189/172756505781829584, 2005.

Glen, J.: The creep of polycrystalline ice, Proc. R. Soc. A, 228, 519–538, 1955.

Glen, J.: The flow law of ice: A discussion of the assumptions made in glacier theory, their experimental foundations and consequences,

30   IASH Publ, 47, 171–183, 1958.

Glen, J. W.: Experiments on the deformation of ice, J. Glaciol., 2, 111–114, 1952.

Glen, J. W.: Rate of flow of polycrystalline ice, Nature, 172, 721–722, 1953.

Gödert, G.: A mesocopic approach for modelling texture evolution of polar ice including recrystallisation phenomena, Ann. Glaciol., 37, 23–28, doi:10.3189/172756403781815375, 2003.

35 Greve, R.: Application of a polythermal three-dimensional ice sheet model to the Greenland Ice Sheet: Response to steady-state and transient climate scenarios, J. Clim., 10, 901–918, 1997.

Greve, R. and Blatter, H.: Dynamics of Ice Sheets and Glaciers, Advances in Geophysical and Environmental Mechanics and Mathematics, Springer-Verlag, 2009.

Greve, R. and Blatter, H.: Comparison of thermodynamics solvers in the polythermal ice sheet model SICOPOLIS, Polar Science, 10, 11 – 23, doi:http://dx.doi.org/10.1016/j.polar.2015.12.004, 2016.

5 Hulbe, C. L., Wang, W., Joughin, I. R., and Siegert, M. J.: The role of lateral and vertical shear in tributary flow toward a West Antarctic ice stream, Ann. Glaciol., 36, 244–250, 2003.

Hutter, K.: Dynamics of glaciers and large ice masses, Ann. Rev. Fluid Mech., 14, 87–130, 1982.

Jacka, T. and Maccagnan, M.: Ice crystallographic and strain rate changes with strain in compression and extension, Cold Regions Science and Technology, 8, 269–286, 1984.

10 Jaeger, J. C.: Elasticity, fracture and flow: with engineering and geological applications, Methuen, 3rd edn., 1969.

Kamb, B.: Experimental recrystallization of ice under stress, American Geophysical Union, 1973.

Larour, E., Seroussi, H., Morlighem, M., and Rignot, E.: Continental scale, high order, high spatial resolution, ice sheet modeling using the Ice Sheet System Model (ISSM), J. Geophys. Res., 117, 1–20, doi:10.1029/2011JF002140, 2012.

Li, J. and Jacka, T.: Correspondence. Horizontal shear rate of ice initially exhibiting vertical compression fabrics, J. Glaciol., 44, 670–672,
15   1998.

Li, J., Jacka, J., and Budd, W. F.: Deformation rates in combined compression and shear for ice which is initially isotropic and after the development of strong anisotropy, Ann. Glaciol., 23, 247–252, 1996.

Lile, R.: The effect of anisotropy on the creep of polycrystalline ice, J. Glaciol., 21, 475–483, 1978.

Lliboutry, L.: Anisotropic, transversely isotropic nonlinear viscosity of rock ice and rheological parameters inferred from homogenization,
20   International Journal of Plasticity, 9, 619–632, 1993.

Ma, Y., Gagliardini, O., Ritz, C., Gillet-Chaulet, F., Durand, G., and Montagnat, M.: Enhancement factors for grounded ice and ice shelves inferred from an anisotropic ice-flow model, J. Glaciol., 56, 805–812, 2010.

MacAyeal, D.: Large-scale ice flow over a viscous basal sediment: Theory and application to Ice Stream B, Antarctica, J. Geophys. Res., 94, 4071–4087, 1989.

25 Martín, C. and Gudmundsson, G. H.: Effects of nonlinear rheology, temperature and anisotropy on the relationship between age and depth at ice divides, The Cryosphere, 6, 1221–1229, doi:10.5194/tc-6-1221-2012, 2012.

Martin, M. A., Winkelmann, R., Haseloff, M., Albrecht, T., Bueler, E., Khroulev, C., and Levermann, A.: The Potsdam Parallel Ice Sheet Model (PISM-PIK) - Part 2: Dynamic equilibrium simulation of the Antarctic ice sheet, The Cryosphere, 5, 727–740, doi:10.5194/tc-5-727-2011, 2011.

30 Montagnat, M., Azuma, N., Dahl-Jensen, D., Eichler, J., Fujita, S., Gillet-Chaulet, F., Kipfstuhl, S., Samyn, D., Svensson, A., and Weikusat, I.: Fabric along the NEEM ice core, Greenland, and its comparison with GRIP and NGRIP ice cores, The Cryosphere, 8, 1129–1138, doi:10.5194/tc-8-1129-2014, 2014.

Morgan, V., van Ommen, T., Elcheikh, A., and Li, J.: Variations in shear deformation rate with depth at Dome Summit South, Law Dome, East Antarctica, Ann. Glaciol., pp. 135–139, 1998.

35 Morland, L. and Zainuddin, R.: Plane and radial ice-shelf flow with prescribed temperature profile., In Veen, C.J. van der, and Oerlemans, J., eds. Dynamics of the West Antarctica Ice Sheet. Proceedings of a Workshop held in Utrecht, May 6-8, 1985. Dordrecht, D. Rediel Publishing Company, 117, 117–140, 1987.

Nye, J. F.: The flow law of ice from measurements in glacier tunnels, laboratory experiments and the Jungfraufirn borehole experiment, Proc. R. Soc. A, 219, 477–489, 1953.

Parizek, B. R. and Alley, R. B.: Implications of increased Greenland surface melt under global-warming scenarios: ice-sheet simulations, Quat. Sci. Rev., 23, 1013–1027, 2004.

5   Paterson, W.: The Physics of Glaciers, Pergamon Press, Oxford, London, New York, 3rd edn., 1994.

Pattyn, F.: A new three-dimensional higher-order thermomechanical ice sheet model: Basic sensitivity, ice stream development, and ice flow across subglacial lakes, J. Geophys. Res., 108, 1–15, doi:10.1029/2002JB002329, 2003.

Pattyn, F., Perichon, L., Aschwanden, A., Breuer, B., De Smedt, B., Gagliardini, O., Hindmarsh, R., Hubbard, A., Johnson, J., Kleiner, T., Konovalov, Y., Martin, C., Payne, T., Pollard, D., Price, S., Saito, F., and Sugiyama, S.: ISMIP-HOM: Results of the Higher-Order Ice

10   Sheet Model Intercomparison Project, in: European Geosciences Union, 2007.

Pattyn, F., Perichon, L., Aschwanden, A., Breuer, B., de Smedt, B., Gagliardini, O., Gudmundsson, G. H., Hindmarsh, R. C. A., Hubbard, A., Johnson, J. V., Kleiner, T., Konovalov, Y., Martin, C., Payne, A. J., Pollard, D., Price, S., Rückamp, M., Saito, F., Soucek, O., Sugiyama, S., and Zwinger, T.: Benchmark experiments for higher-order and full-Stokes ice sheet models (ISMIP-HOM), The Cryosphere, 2, 95–108, 2008.

15   Pettit, E., Thorsteinsson, T., Jacobson, H., and Waddington, E.: The role of crystal fabric in flow near an ice divide, J. Glaciol., 53, 277–288, doi:10.3189/172756507782202766, 2007.

Pimienta, P., Duval, P., and Lipenkov, V. Y.: Mechanical behaviour of anisotropic polar ice, in: The Physical Basis of Ice Sheet Modelling, pp. 57–65, IAHS Publ. 170, 1987.

Placidi, L., Greve, R., Seddik, H., and Faria, S.: Continuum-mechanical, Anisotropic Flow model, for polar ice masses, based on an

20   anisotropic Flow Enhancement factor, Continuum Mech. Thermodyn., 22, 221–237, doi:10.1007/s00161-009-0126-0, 2010.

Russell-Head, D. and Budd, W.: Ice-sheet flow properties derived from bore-hole shear measurements combined with ice-core studies, J. Glaciol., 24, 117–130, 1979.

Schmid, E. and Boas, W.: Plasticity of crystals, F.A. Hughes and Co. Ltd., London, 1950.

Seddik, H., Greve, R., Zwinger, T., and Placidi, L.: A full Stokes ice flow model for the vicinity of Dome Fuji, Antarctica, with induced

25   anisotropy and fabric evolution, The Cryosphere, 5, 495–508, doi:10.5194/tc-5-495-2011, 2011.

Staroszczyk, R. and Gagliardini, O.: Two orthotropic models for strain-induced anisotropy of polar ice, J. Glaciol., 45, 485–494, 1999.

Tarasov, L. and Peltier, W. R.: A geophysically constrained large ensemble analysis of the deglacial history of the North American ice-sheet complex, Quat. Sci. Rev., 23, 359=388, 2004.

Thorsteinsson, T.: An analytical approach to deformation of anisotropic ice-crystal aggregates, J. Glaciol., 47, 507–516, 2001.

30   Thorsteinsson, T.: Fabric development with nearest-neighbour interaction and dynamic recrystallization, J. Geophys. Res. - Solid Earth, 107, doi:10.1029/2001JB000244, 2002.

Treverrow, A., Budd, W. F., Jacka, T. H., and Warner, R. C.: The tertiary creep of polycrystalline ice: experimental evidence for stress-dependent levels of strain-rate enhancement, J. Glaciol., 58, 301–314, doi:10.3189/2012JoG11J149, 2012.

Treverrow, A., Warner, R. C., Budd, W. F., Jacka, T. H., and Roberts, J. L.: Modelled stress distributions at the Dome Summit South borehole,

35   Law Dome, East Antarctica: a comparison of anisotropic ice flow relations, J. Glaciol., 61, 987–1004, doi:13.3189/2016JoG14J198, 2015.

Trickett, Y., Baker, I., and Pradhan, P.: The orientation dependence of the strength of ice single crystals, J. Glaciol., 46, 41–44, doi:10.3189/172756500781833296, 2000.

van der Veen, C. J. and Whillans, I. M.: Development of fabric in ice, Cold Reg. Sci. Technol., pp. 171–195, doi:10.1016/0165-232X(94)90027-2, 1994.

Wang, W. and Warner, R. C.: Modelling of anisotropic ice flow in Law Dome, East Antarctica, Ann. Glaciol., 29, 184–190, 1999.

Wang, W., Warner, R. C., and Budd, W. F.: Ice-flow properties at Dome Summit South, Law Dome, East Antarctica, Ann. Glaciol., 35, 567–573, 2002a.

Wang, W., Jun, L., Zwally, H. J., Morgan, V., and van Ommen, T. D.: The effect of anistropic flow properties on ice-sheet surface elevation change, Ann. Glaciol., 39, 439–444, 2004.

Wang, W., Li, J., and Zwally, H. J.: Dynamic inland propagation of thinning due to ice loss at the margins of the Greenland ice sheet, J. Glaciol., 58, 734–740, doi:10.3189/2012JoG11J187, 2012.

Wang, W. L. and Warner, R. C.: Simulation of the influence of ice rheology on velocity profiles and ice-sheet mass balance, Ann. Glaciol., 27, 194–200, 1998.

Wang, W. L., Zwally, H. J., Abdalati, W., and Luo, S.: Modeling of ice flow and internal layers along a flowline through Swiss Camp, West Greenland, Ann. Glaciol., 34, 303–308, 2002b.

Wang, W. L., Zwally, H. J., Hulbe, C. L., Siegert, M. J., and Joughin, I. R.: Anisotropic ice flow leading to the onset of Ice Stream D, West Antarctica: numerical modelling based on the observations from Byrd Station borehole, Ann. Glaciol., 37, 397–403, 2003.

Warner, R. C., Jacka, T. H., Li, J., and Budd, W. F.: Tertiary flow relations for compression and shear components in combined stress tests on ice, in: Advances in cold-region thermal engineering and sciences: technological, environmental, and climatological impact, edited by Hutter, K., Wang, Y., and Beer, H., pp. 259–270, Springer-Verlag, 1999.

Weertman, J.: Deformation of floating ice shelves, J. Glaciol., 3, 38–42, 1957.

Zwinger, T., Schäfer, M., Martín, C., and Moore, J. C.: Influence of anisotropy on velocity and age distribution at Scharffenbergbotnen blue ice area, The Cryosphere, 8, 607–621, doi:10.5194/tc-8-607-2014, 2014.
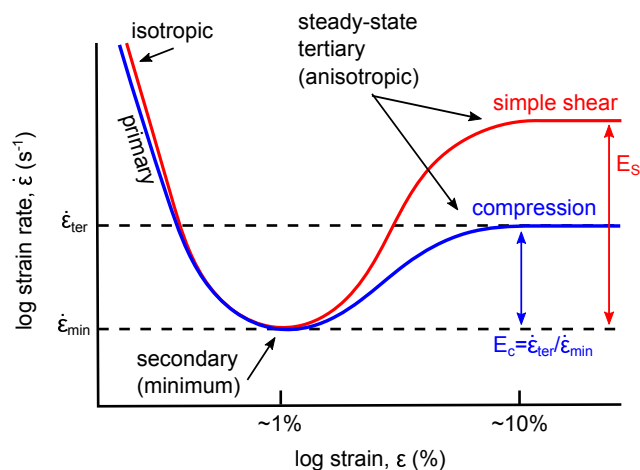
Figure 1. Strain rate characteristics of polycrystalline ice undergoing deformation driven by single stresses as measured in laboratory experiments. The part of the curve corresponding to tertiary (steady-state) anisotropic creep is relevant to the deformation of ice masses in typical ice sheets and glaciers. The red (blue) curve illustrates the result of simple shear-alone (compression-alone) stress configurations. Note that the ratio of the shear enhancement factor E_S to the compression enhancement factor E_C is approximately $8/3$, and the enhancement due to compression-alone is approximately three times that of the secondary (minimum) creep rate.

Table 1. Computational times for full Stokes simulations of the embayed ice shelf (section 5.1) using Glen and ESTAR for increasing mesh resolution. The model is simulated for 1 month and for a total of 833 time steps in each case. Dof stands for model degrees of freedom.

Dof	Vertices	CPUs	Glen walltime (s)	ESTAR walltime (s)
2210	10040	16	9084	9281
2760	15665	32	10467	10778
3310	22540	64	12920	13008
4410	40040	128	20852	21008
8820	80080	256	59057	59934
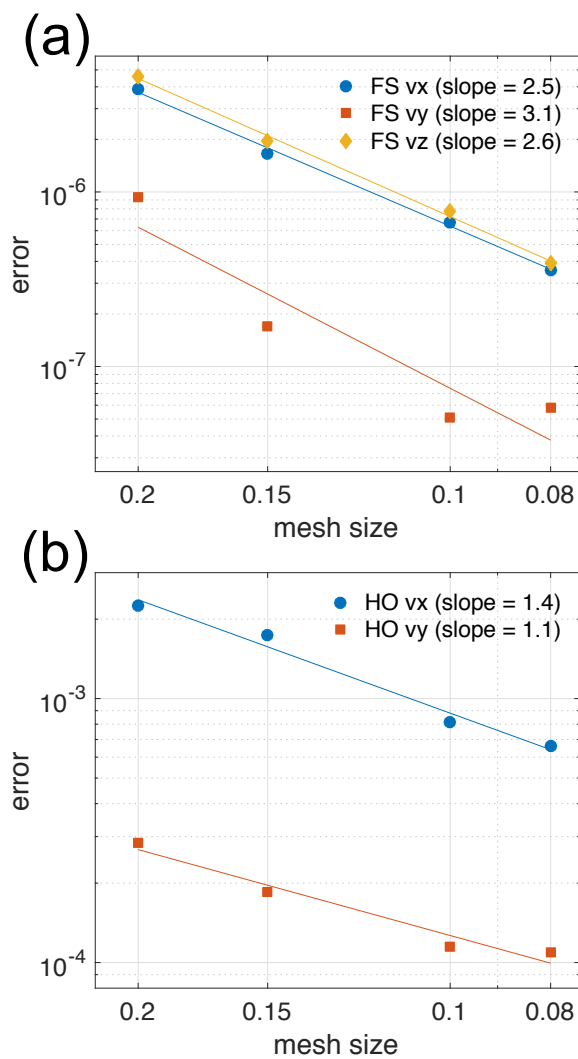
Figure 2. Convergence rates of the simulated **(a)** full Stokes (FS) and **(b)** higher order (HO) velocity fields (v_x, v_y, v_z) to the analytical solutions in Eqs. 13-17 for increasing mesh resolutions.
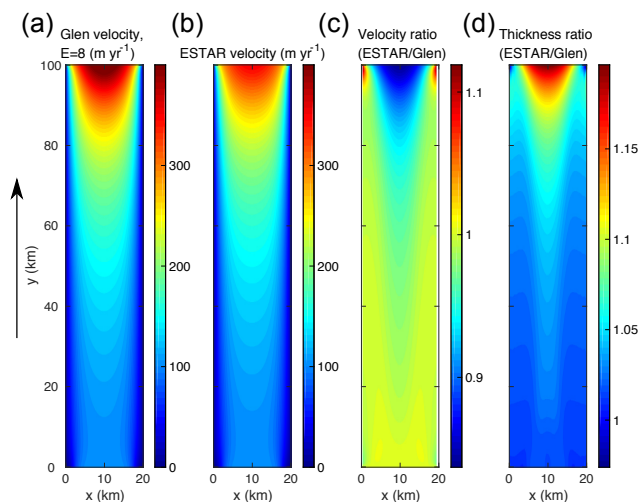
Figure 3. Rectangular ice shelf HO surface velocity magnitudes (m yr^{-1}) using **(a)** Glen and **(b)** ESTAR, and the corresponding ratios (i.e., ESTAR/Glen) between the steady-state **(c)** velocities and **(d)** thicknesses. The black arrow indicates the direction of flow.
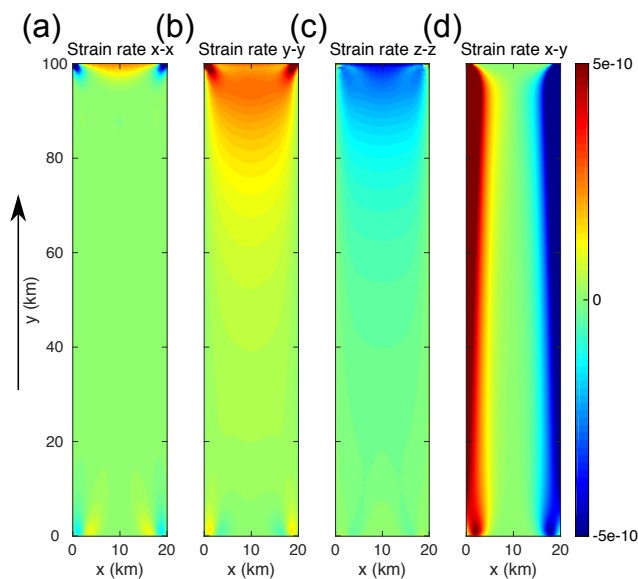
Figure 4. Rectangular ice shelf ESTAR HO surface strain rates (s^{-1}): **(a)** $\dot{\varepsilon}_{xx}$, **(b)** $\dot{\varepsilon}_{yy}$, **(c)** $\dot{\varepsilon}_{zz}$, and **(d)** $\dot{\varepsilon}_{xy}$.
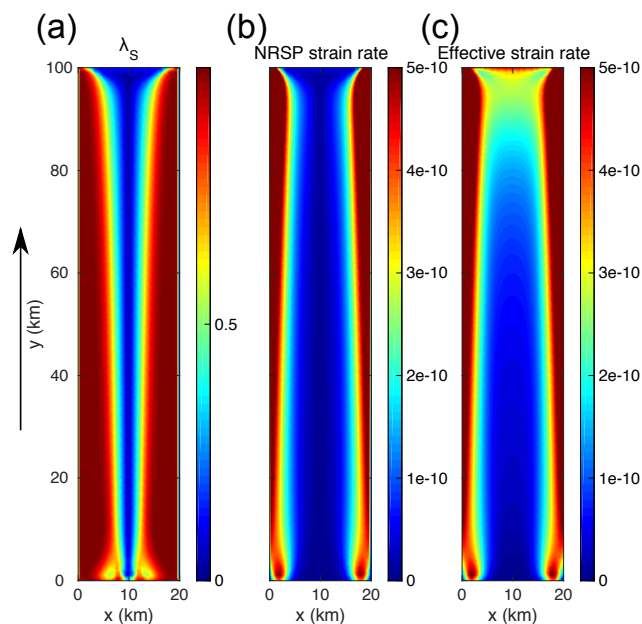
Figure 5. (a) The ESTAR shear ratio λ_S; **(b)** the shear strain rate resolved on the non-rotating shear plane (NRSP) $\dot{\varepsilon}'$ (s^{-1}); and **(c)** the effective strain rate $\dot{\varepsilon}_e$ (s^{-1}). The black arrow indicates the direction of flow. In each case, the surface fields for the HO model are shown.
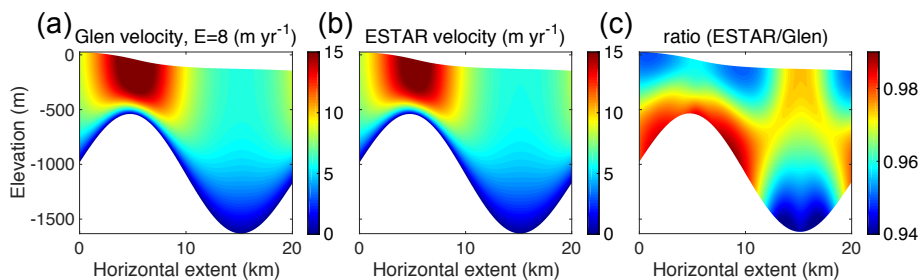
Figure 6. FS steady-state (prognostic) along-flow velocities (v_x) for ISMIPB. **(a)** v_x (m yr^{-1}) for the Glen flow relation with $E_G = 8$; **(b)** v_x (m yr^{-1}) for ESTAR with $E_S = 8$ and $E_C = 3$; and **(c)** ratio between the Glen and ESTAR v_x fields.
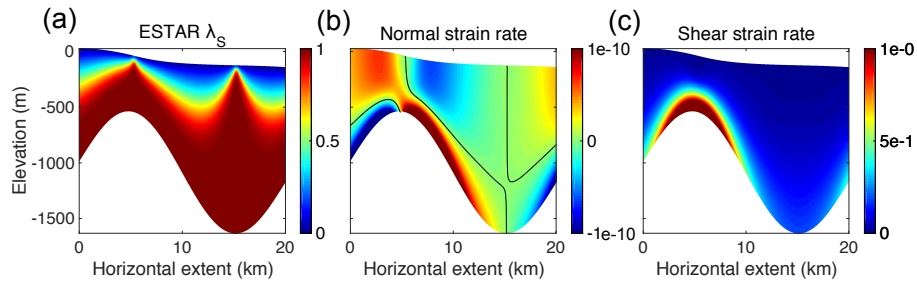
Figure 7. Enhancement factors and normal and shear strain rates for the ISMIPB FS steady-state simulations. **(a)** Shear enhancement factor λ_S (Eq. 6); **(b)** normal strain rate (i.e., $x-x$ strain rate; s^{-1}); and **(c)** shear strain rate (i.e., $x-z$ strain rate; s^{-1}). The black contours in **(b)** correspond to the curves where $\dot{\epsilon}_{xx} = 0$.
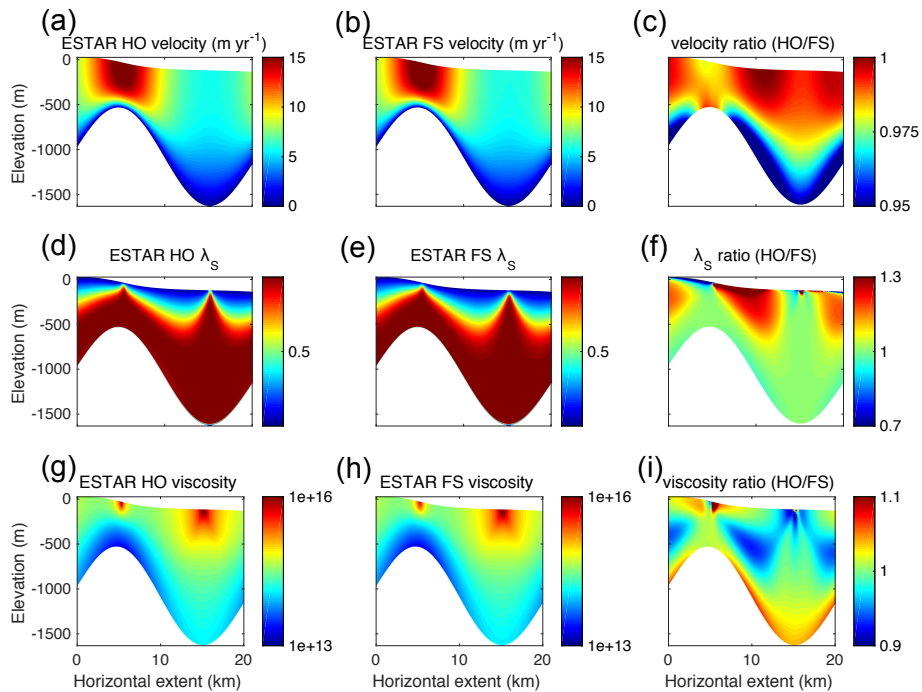
Figure 8. Steady-state (prognostic) results for ISMIPB HO and FS models. **(a)**-**(b)** HO and FS along-flow velocities (v_x; m yr^{-1}), respectively; **(c)** ratio of the deformation velocities (HO/FS); **(d)**-**(e)** HO and FS enhancement factors λ_S, respectively, with their ratio in **(f)**; and **(g)**-**(h)** final HO and FS viscosities (μ; Pa s), with their ratio in panel **(i)**.
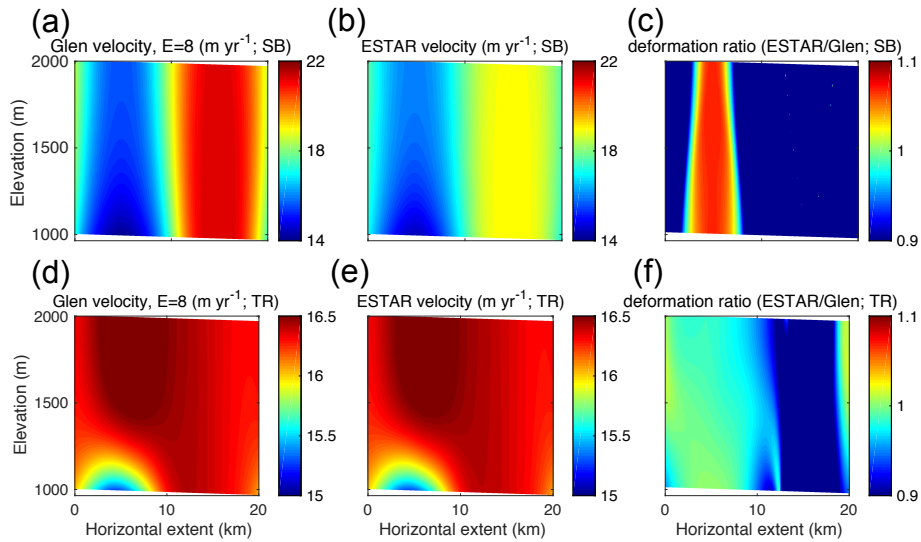
Figure 9. ISMIPD FS diagnostic (stress balance – SB; **(a)**-**(c)**) and prognostic (transient – TR; **(d)**-**(f)**) along-flow velocities (v_x). **(a)** and **(d)** Glen SB and TR v_x, respectively; **(b)** and **(e)** ESTAR SB and TR v_x, respectively; and **(c)** and **(f)** ratios of Glen to ESTAR SB and TR deformation velocities (i.e., the difference between v_x and the sliding velocity, which is taken to be equal to the velocity along the basal mesh points).
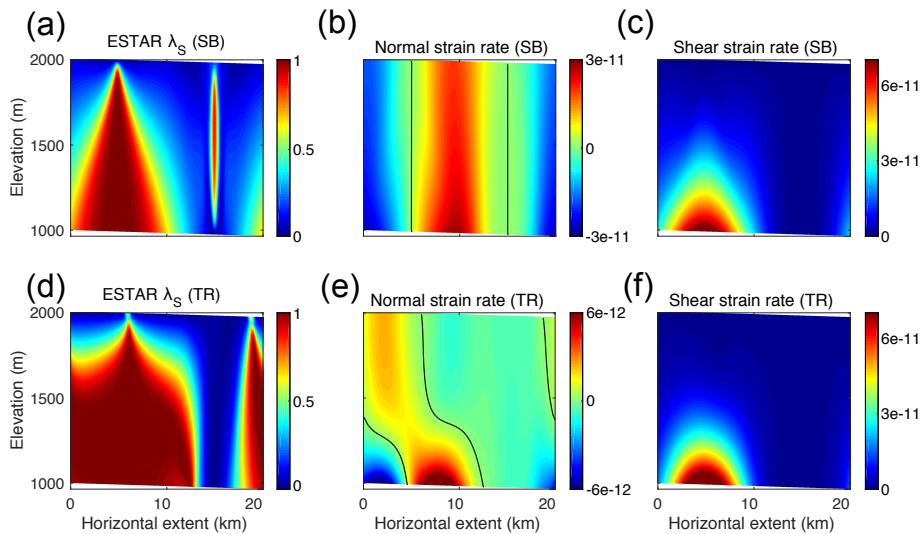
Figure 10. ISMIPD ESTAR FS SB and TR enhancement factors and normal and shear strain rates. **(a)**-**(d)** SB and TR λ_S; **(b)**-**(e)** SB and TR normal strain rates; and **(c)**-**(f)** SB and TR shear strain rates. The black contour lines in **(b)** and **(e)** correspond to the curves where $\dot{\epsilon}_{xx} = 0$.